Depth of faulting and ancient heat flows in the Kuiper region of Mercury from lobate scarp topography

Isabel Egea-González [a,*], Javier Ruiz [b], Carlos Fernández [c], Jean-Pierre Williams [d], Álvaro Márquez [e], Luisa M. Lara [a]

[a] Instituto de Astrofísica de Andalucía, CSIC, Glorieta
[b] Departamento de Geodinámica, Facultad de Ciencias Geológicas, Universidad Complutense de Madrid, 28040 Madrid, Spain
[c] Departamento de Geodinámica y Paleontología, Universidad de Huelva, Campus de El Carmen, 21071 Huelva, Spain
[d] Department of Earth and Space Sciences, University of California, Los Angeles, CA 90095, USA
[e] Área de Geología, Universidad Rey Juan Carlos, Móstoles, Madrid, Spain

ABSTRACT

Mercurian lobate scarps are interpreted to be the surface expressions of thrust faults formed by planetary cooling and contraction, which deformed the crust down to the brittle–ductile transition (BDT) depth at the time of faulting. In this work we have used a forward modeling procedure in order to analyze the relation between scarp topography and fault geometries and depths associated with a group of prominent lobate scarps (Santa Maria Rupes and two unnamed scarps) located in the Kuiper region of Mercury for which Earth-based radar altimetry is available. Also a backthrust associated with one of the lobate scarps has been included in this study. We have obtained best fits for depths of faulting between 30 and 39 km; the results are consistent with the previous results for other lobate scarps on Mercury.

The so-derived fault depths have been used to calculate surface heat flows for the time of faulting, taking into account crustal heat sources and a heterogeneous surface temperature due to the variable insolation pattern. Deduced surface heat flows are between 19 and 39 mW m^{-2} for the Kuiper region, and between 22 and 43 mW m^{-2} for Discovery Rupes. Both BDT depths and heat flows are consistent with the predictions of thermal history models for the range of time relevant for scarp formation.

Keywords:
Mercury
Lobate scarps
Depth of faulting
Brittle–ductile transition
Heat flow

1. Introduction

The most representative tectonic features of Mercury are lobate scarps, which are characterized by a steeply rising scarp face, a gently declining back scarp and a trailing syncline (Strom et al., 1975; Cordell and Strom, 1977; Melosh and McKinnon, 1988; Watters et al., 2001, Watters and Nimmo, 2010), and were mostly formed in the Tolstojan and Calorian periods (Watters and Nimmo, 2010), corresponding to an age between 3.2 and 4 Gyr (e.g., Tanaka and Hartmann, 2008). Lobate scarps are interpreted to be the surface expressions of thrust faults formed by planetary cooling and contraction (e.g., Strom et al., 1975) and estimates of their depth of faulting suggest that they deformed the crust down to the brittle–ductile transition (BDT) depth at the time of fault formation, providing important clues about the geological and thermal history of Mercury (Watters et al., 2002; Nimmo and Watters, 2004).

Watters et al. (2002) obtained a depth of faulting of 35–40 km for Discovery Rupes, a prominent lobate scarp imaged by Mariner 10, using a forward modeling procedure for fitting the topography above a thrust fault to stereographically deduced topography. Recently, Ritzer et al. (2010) obtained a depth of faulting of 35 km for two lobate scarps located near the equator using a similar procedure and a topographic profile deduced from the Mercury Laser Altimeter (MLA) onboard the MESSENGER spacecraft. The so-obtained depths of faulting provide constraints on the mechanical and thermal properties of the lithosphere at the time when the lobate scarps were formed (e.g., Schultz and Watters, 2001; Grott et al., 2007; Ruiz et al., 2008). Watters et al. (2002) deduced surface heat flows of 10–43 mW m^{-2} from the depth of faulting beneath Discovery Rupes using a linear thermal gradient and assuming a wide range of temperatures at the BDT. Nimmo and Watters (2004) derived an upper limit of 50 mW m^{-2} for the mantle heat flow using the BDT depths calculated by Watters et al. (2002), a strength envelope procedure and considering heat generation within the crust. The obtained BDT depths and heat flows can be compared with predictions from thermal history models (e.g., Hauck et al., 2004; Williams et al., 2011) in order to further constraint the thermal history of Mercury.

In this work we use a forward modeling procedure in order to analyze fault geometries and depths associated with a group of

* Corresponding author. Tel.: +34 958121566; fax: +34 958814530.
E-mail address: isaegea@iaa.es (I. Egea-González).

prominent lobate scarps located in the Kuiper region of Mercury for which Earth-base radar topographic profiles are available (Harmon et al., 1986): Santa Maria Rupes and two unnamed lobate scarps referred to as S_K3 and S_K4 scarps. Calculations of surface heat flow have been performed from the BDT depth beneath these lobate scarps (and beneath Discovery Rupes for comparison) by assuming heat sources homogeneously distributed in the crust. Crustal heat sources abundances are based on preliminary surface measurements of Th and K performed with the MESSENGER Gamma-Ray Spectrometer (GRS) (Peplowsky et al., 2011). Indeed, previous works have pointed out the importance of taking into account crustal heat sources in this kind of calculations, since the obtained surface heat flow increases with the proportion of heat sources within the crust (Ruiz et al., 2006, 2009). Finally, we discuss the implications of our results for the history of Mercury.

2. Topographic profiles

Santa Maria Rupes (3.5°N, 19°W), and the scarps S_K3 (10.3°N, 13°W) and S_K4 (4°N, 15°W) are three lobate scarps situated in the same region of the Kuiper's quadrangle. These three lobate scarps have similar features: all of them are over 200 km long, have a relief of ~700 m and the associated thrust faults dip to the west (Fig. 1a and b). To the west of the S_K4 scarp we identify another structure, which runs parallel. Offset of the walls and floors of transected impact craters suggest that this structure is also a thrust fault (Fig. 2), which dips to the east and is ~200 km long, and could be a backthrust associated with the S_K4 scarp.

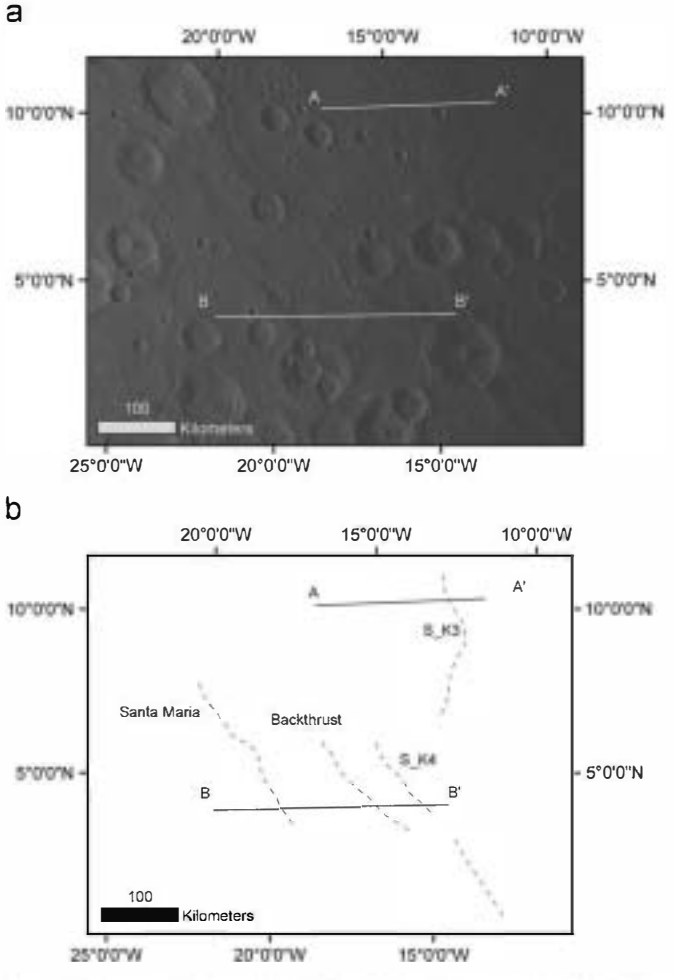

Fig. 1. (a) Mariner 10 mosaic showing the location of the Arecibo radar altimetry profiles (Harmon et al., 1986) used in this study. (b) This map shows the location of the Santa Maria Rupes, S_K4 and S_K3 scarps (dashed lines). Solid lines indicate the trace of the topographic profiles.

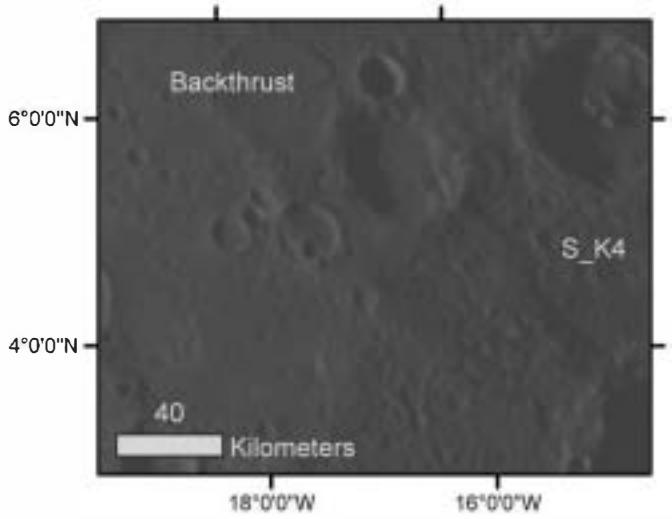

Fig. 2. Detailed vision of the backthrust fault associated to the S_K4 scarp. The backthrust crosscuts slightly shortens two impact craters.

Topographic profiles across these three scarps have been derived by applying the delay-Doppler method to the data obtained from the Arecibo antenna in the period 1978 –1984 (Harmon et al., 1986). These authors collated overlapping profiles and averaged them over 0.15° longitude bins to produce a single profile with surface resolutions of 0.15° and 2.5° in longitude and latitude, respectively (i.e., 6.4×106 km). The altitude resolution of the topographic profiles is variable, usually lower than 50 m for the S_K3 scarp, ~100 m for the S_K4 scarps, but very variable for Santa Maria Rupes, with resolutions ranging from ~50 to ~400 m.

Fig. 1a and b shows our four faults and the locations of topographic profiles used in the model. The topographic profile across the S_K3 scarp, A–A′, is situated between 12.0°W, 10.4°N and 17.1°W, 10.0°N; Santa Maria Rupes and the S_K4 scarp are crossed by a profile, B–B′, located between 14.4°W, 3.9°N and 21.6°W, 3.9°N. Topographic profiles across Santa Maria Rupes, and the S_K4 and S_K3 scarps exhibit a regional slope towards the west. The origin of this slope is beyond the scope of this work, so we filter the regional slope to obtain detrended topography, which is used for forward modeling. Inspection of the topography suggests that a simple linear detrending is sufficiently accurate in this case. The topographic profile across Santa Maria Rupes shows a small impact crater in the back of the lobate scarp. This crater produces a low area, postdating fault, in the back of the scarp. To obtain the fault geometry we have restored crater effects and the low area has not been considered.

3. Depth of faulting

In this section we use the topographic profiles described in the previous section and a forward modeling procedure to analyze fault displacements, dip angles and depths of faulting of the analyzed lobate scarps. We use the mechanical dislocation program Coulomb (Lin and Stein, 2004; Toda et al., 2005; available online at http://earthquake.usgs.gov/research/modeling/coulomb/download.php) to predict the surface displacement associated with faulting. This program has been previously used to study thrust faults beneath

lobate scarps on Mars (Schultz and Watters, 2001; Ruiz et al., 2008) and Mercury (Watters et al., 2002).

Coulomb models the lithosphere assuming an elastic homogeneous and isotropic half-space. A range of significant parameters such as dip angle, vertical depth of faulting, magnitude and sense of offset along the fault and elastic constants are specified in the model. Then the material displacements are determined and comparison of the topographic profiles with the predicted topography above a given fault allows us to identify a narrow range of admissible fault dips, depths and displacements. For the values of the elastic parameters, we assumed Young's modulus of 100 GPa and Poisson's ratio of 0.25 (Hauck et al., 2004). Reasonable variations in these parameters do not produce significant variations in the results (see also Watters et al., 2002; Grott et al., 2007; Ritzer et al., 2010).

Different profile orientations across a fault result in different cross-sectional surface topographies. The width of a lobate scarp is especially sensitive to the orientation of the profile relative to the scarp's strike and can introduce error into the estimate of the faulting depth. For this reason, we have used a geographic information system (GIS) to account for the relative positions between the profile used and the modeled faults. Coulomb provides an output that let us calculate the simulated coordinates of a grid of points in the area where the fault is placed. These coordinates can be introduced in a GIS and we can use its tools to obtain the topographic profile with the required orientation. We have used a sinusoidal projection to avoid distortion, as our area of interest is small and placed near the equator. The predicted topography is also influenced by the distribution of relative displacement along the fault. Here we use an elliptic tapered slip distribution, with a linear taper to within 10 km of faults tips to avoid stress singularities (Schultz and Watters, 2001; Ruiz et al., 2008).

Best fits are determined by calculating the L^2-norm of the difference between measured and simulated topography. L^2-norm is defined as

$$f(x)-g(x)_2 = \left(\int_a^b (f(x)-g(x))^2 \, dx \right)^{1/2}, \quad (1)$$

where $f(x)$ and $g(x)$ are the observed and simulated profiles, respectively; a and b are the boundaries of the topographic profiles. In order to measure the difference between profiles, we perform a numerical integration discretizing the profile in k points n_i and we divide by the total length of the profile $L=n_k-n_1$ to normalize the norm. We obtain the expression:

$$\frac{1}{L}\|f(x)-g(x)\|_2 = \left[\frac{1}{n_k-n_1} \left(\sum_{i-1}^{k-1} |n_{i+1}-n_i| R_i^2 \right) \right]^{1/2} \quad (2)$$

where R_i is the difference between the observed and modeled topography at the point n_i.

Our results are summarized in Table 1. The best fits to the topography across Santa Maria Rupes are obtained using depth of faulting of 36–39 km, fault dip angle of 28°–32° and displacement 1.0–1.1 km. In these ranges of values we have found combinations of parameters that provide modeled profiles with similar, low error values. Fig. 3 shows the topographic profile and modeled profiles belonging to the solution range. Changing the fault geometry to a listric shape leads to unacceptable fits. Elastic dislocation modeling of the primary structure in S_K4 Rupes neglecting the backthrust suggests a depth of faulting of 37–40 km, a dip angle of 43°–53° and a displacement of 0.9–1.0 km. However, dip angles above 45° are unexpected in thrust faults (Turcotte and Schubert, 2002). By including a backthrust in the model errors are reduced, and dip angles in agreement with typical thrust faults are obtained. The fault beneath scarp S_K4 including the backthrust is best fit by models with displacements of 1.0–1.1, dip angles 40°–44° and depths of faulting 30–36 km (Fig. 3). The backthrust is a fault with an upper edge between 0 and 0.5 km deep and fault depths of 10–15 km, dip angles of 18°–25° and displacement of 0.9–1.0 km. The best fits for S_K3 are obtained for displacements of 1.0–1.2 km, dip angles of 22°–28° and depth of faulting of 33–38 km (Fig. 4). The radar profile across the S_K3 scarp is relatively symmetric, whereas lobate scarps are usually asymmetric in cross-section (Strom et al., 1975; Watters et al., 2001; Watters and Nimmo, 2010); this could indicate complex fault geometry beneath the S_K3 scarps. Because of this symmetric profile, even lower error values provide unacceptably poor fits to the topography. Therefore, this method has not been used in this fault and best matches have been qualitatively estimated.

Summarizing, we obtain best fits to the observed topographies of lobate scarps in the Kuiper region of Mercury for thrust fault depths of 30–39 km. This result is consistent with the depth of faulting of 35–40 km obtained by Watters et al. (2002) for Discovery Rupes, and of 35 km obtained by Ritzer et al. (2010) for two unnamed lobate scarps located near the equator at 59.3°E and 64.7°E.

Table 1
Results of mechanical modeling.

Feature	Displacement (km)	Dip	Depth of burial (km)	Depth of faulting (km)
Santa Maria Rupes	1.0–1.1	28°–32°	0.0	36–39
S K4 scarp	1.0–1.1	40°–44°	0.0	30–36
S K4 backthrust	0.9–1.0	18°–25°	0–0.5	10–15
S K3 scarp	1.0–1.2	22°–28°	0.0	33–38

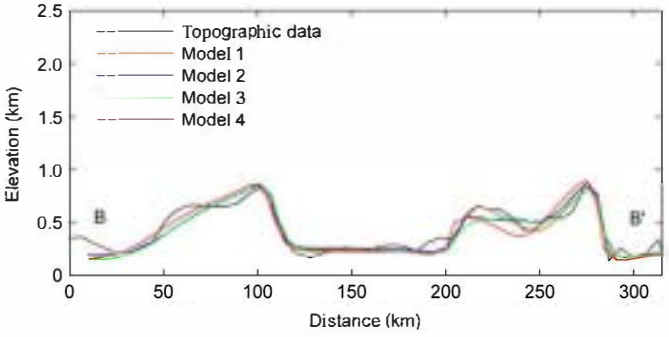

Fig. 3. Comparison of modeled profiles in our range of solutions and topographic profile across Santa Maria Rupes and S K4. Model 1 is the best fit model for the topography of Santa María Rupes and S K4 scarps, its error value is 2969 m; this model shows a geometry with a displacement (D) of 1.0 km, a dip (δ) of 31°, and a depth of faulting (T) of 38 km for the thrust fault beneath Santa Maria Rupes. S K4 scarp is modeled with $D=1.1$ km, $\delta=44°$ and $T=30$ km. The backthrust associated to the S K4 scarp has $D=0.9$ km, $\delta=23°$ and $T=15$ km, and the upper edge is 0.5 km deep. Models 2–4 show suitable profiles with errors values between 2977 and 3020 m. These models are calculated with geometries included in our ranges of valid parameters:

Model 2 Santa Maria: $D=1.0$ km, $\delta=30°$, $T=37$ km. S K4: $D=1.1$ km, $\delta=42°$, $T=33$ km. Backthrust: $D=1.0$ km, $\delta=20°$, $T=12$ km.
Model 3 Santa Maria: $D=1.1$ km, $\delta=28°$, $T=36$ km. S K4: $D=1.0$ km, $\delta=40°$, $T=36$ km. Backthrust: $D=1.0$ km, $\delta=18°$, $T=10$ km.
Model 4 Santa Maria: $D=1.1$ km, $\delta=29°$, $T=39$ km. S K4: $D=1.0$ km, $\delta=43°$, $T=34$ km. Backthrust: $D=0.9$ km, $\delta=25°$, $T=12$ km.

4. Heat flow

Thrust faults beneath lobate scarps are considered to deform the entire brittle crust, and therefore the temperature at the BDT

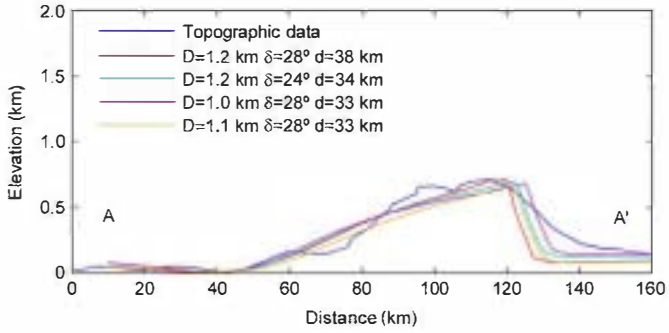

Fig. 4. Comparison of a group of predicted structural relieves and measured topography across the S K3 scarp.

depth (T_{BDT}) can be estimated from the temperature dependence of ductile strength by equating the brittle and ductile strength for the depth $z=z_{BDT}$ (where z_{BDT} is the depth to the brittle–ductile transition). The brittle strength is calculated for zero pore pressure according to

$$(\sigma_1-\sigma_3)_b=\alpha\rho g z, \tag{3}$$

where ρ is the density, g is the acceleration due to the gravity (3.7 m s^{-2} for Mercury), z is the depth and α is a coefficient depending on the stress regime (which is 3 for pure compression, appropriate for thrust faulting; e.g., Ranalli, 1997). The ductile strength is given by

$$(\sigma_1-\sigma_3)_d=\left(\frac{\dot{\varepsilon}}{A}\right)^{1/n}\mathrm{Exp}\left(\frac{Q}{nRT}\right), \tag{4}$$

where $\dot{\varepsilon}$ is the strain rate, A and n are laboratory-determined constants, Q is the activation energy of creep, R=8.31447 J mol^{-1} K^{-1} is the gas constant and T is the absolute temperature. Recent MESSENGER observations suggest that a considerable fraction of the crust of Mercury had a volcanic origin (Head et al., 2008; Denevi et al., 2009), therefore, we use a crustal density of 2900 kg m^{-3} and the flow law of dry Maryland diabase for creep parameters, which are n_c=4.7, Q_c=485 kJ mol^{-1} and A_c=8 MPa$^{-4.7}$ s^{-1} (Mackwell et al., 1998). Strain rates used in our calculations are 10^{-16} s^{-1}, which is a characteristic value for active terrestrial plate interiors (e.g., Tesauro et al., 2007), and 10^{-19} s^{-1}, a typical value for thermal contraction on terrestrial planets (e.g., Schubert et al., 1988).

The estimation of T_{BDT} permits the calculation of the surface heat flow. Previous studies have shown that taking into account crustal heat sources increases the obtained surface heat flows (Ruiz et al., 2006, 2009). Here we assume homogeneously distributed crustal heat sources since heavy cratering should have contributed to mixing the upper crust, and for this reason we use a constant value for the heat production rate. The surface heat flow is then given by

$$F=\frac{k(T_{BDT}-T_S)}{z_{BDT}}+\frac{z_{BDT}H}{2}, \tag{5}$$

where k is the thermal conductivity of the crust, T_s is the surface temperature and H is volumetric heat production rate.

We use a thermal conductivity of 2 W m^{-1} K^{-1} for the entire crust, a value appropriate for basaltic rocks and for a wide variety of Earth crustal rocks at temperatures of several hundreds of degrees centigrade (e.g., Beardsmore and Cull, 2001; Bonner et al., 2003). The volumetric heating rate depends on both the amount of heat producing elements and time before present. In our calculations we use a range of time between 3.2 and 4 Ga, the time period of lobate scarp formation. We adopt thorium and potassium abundances of 0.5–1.9 ppm and 460–1140 ppm, respectively, preliminary values obtained from MESSENGER GRS data (Peplowski et al., 2011), and we estimated U abundance by assuming the chondritic Th/U ratio of 3.6 (Morgan and Anders, 1980; Taylor and Scott, 2005). Therefore, the used crustal heat production rates range between 1.7×10^{-4} and 8.7×10^{-4} mW m^{-3} at the time of scarp formation. The distribution of surface temperatures on Mercury is heterogeneous primarily due to the coupled spin-orbit resonance and relatively high eccentricity ($\sim$0.2) resulting in a strong longitudinal and latitudinal dependence on insolation (see Mitchell and de Pater, 1994; Vasavada et al., 1999; Aharonson et al., 2004). We take into account this effect by assuming a surface temperature of 435 K, a value representative for the location of the three scarps studied here after the present-day surface temperature model of Vasavada et al. (1999).

Fig. 5 shows the surface heat flow as a function of the BDT depth, strain rate and volumetric heat rate. For z_{BDT}=30–39 km, we obtain T_{BDT}=735–819 K and a surface heat flow of 19–39 mW m^{-2}. For comparison, we have calculated a surface heat flow of 22–43 mW m^{-2} for Discovery Rupes following the same procedure but using z_{BDT}=35–40 km (Watters et al., 2002) and T_s=365 K (according to the present-day surface temperature model of Vasavada et al. (1999) for Discovery Rupes' location). Thus, heat flows do not show significant differences between the region of Discovery Rupes and the region studied here. These results are similar to those obtained by employing heat dissipation rates based on compositional models. Surface heat flows obtained using heat-producing elements abundances derived from compositional models

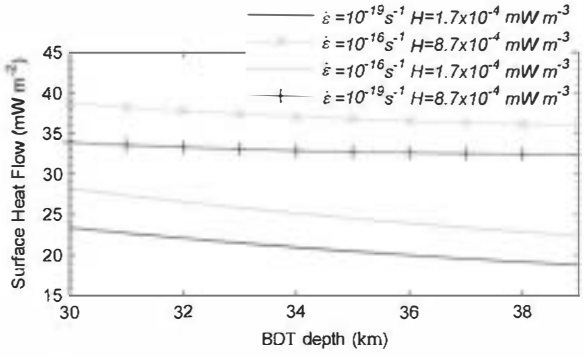

Fig. 5. The obtained surface heat flows for different values of $\dot{\varepsilon}$ and H, shown as a function of the BDT depth.

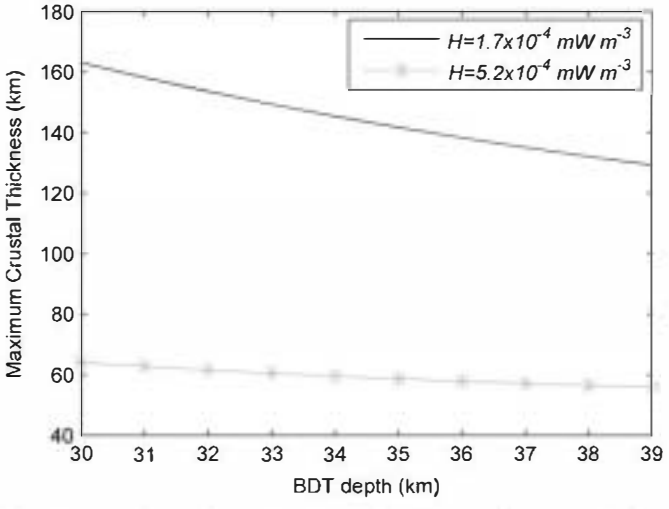

Fig. 6. Maximum permitted crustal thickness as a function of BDT depth and heat dissipation rate, calculated for $\dot{\varepsilon}=10^{-16}$.

Table 2
Heat flow for the Kuiper and the Discovery Rupes regions calculated after the thermal history model methodology described by Williams et al. (2011) for several composition models for Mercury (see Hauck et al., 2004).

Composition model	HPE abundances			Partition of HPE in crust and mantle	Kuiper Region (mW/m^2)		Discovery Rupes (mW/m^2)	
	K (ppm)	U (ppb)	Th (ppb)		3.2 Ga	4.0 Ga	3.2 Ga	4.0 Ga
Condensation model	0	30	120	All in crust	28.1	33.2	28.4	33.5
				Equal partition	28.3	30.9	28.4	31.3
Vaporization model	0	0	400	All in crust	29.1	31.5	29.5	31.7
				Equal partition	29.3	28.6	29.5	29
CI condrite	550	8	30	All in crust	30.2	37.4	30.5	37.8
				Equal partition	28.8	35.2	28.5	35.6

(based on late-stage silicate vaporization, condensation and CI chondritic compositions; see Hauck et al. (2004) for details on heat-producing elements abundances in compositional models) are between 16 and 29 $mW\,m^{-2}$ when usual crustal enrichment factors of 1–4 are applied (see Williams et al., 2011). Our results agree with, although are substantially more restrictive than those found by Watters et al. (2002), 10–43 $mW\,m^{-2}$, though these authors used linear thermal gradients. This is because they used high values of conductivity (3–4 $W\,m^{-1}\,K^{-1}$) and assumed a wider range of T_{BDT} values (300–600 °C).

In addition, our surface heat flow estimations can be used to place constraints on the thickness of the mercurian crust (Ruiz et al., 2008, 2009). If the crustal heat production rates assumed previously are representative for the bulk of the crust, then crustal contribution to the surface heat flow is given by multiplying H by the crustal thickness, and therefore an upper limit on the crustal thickness is imposed by the condition of non-negative mantle heat flow. This upper limit is increased for higher strain rates and lower heat production rates. Thus, we conclude that the maximum permitted crustal thickness is 163 km, and 64 km if we use the average value of H, 5.2×10^{-4} $mW\,m^{-3}$ (Fig. 6). Our results are consistent with crustal thickness <100 km obtained by Smith et al. (2010) from geodetic estimates, and with the maximum crustal thickness (<140 km) calculated by Nimmo and Watters (2004) from fault depth estimates and the absence of melting at the base of the crust.

5. Discussion and conclusions

The depth of faulting obtained for three different regions of Mercury by Watters et al. (2002), Ritzer et al. (2010) and the present work are similar ranging between 30 and 40 km. This could be indicative of a relatively homogeneous depth for the BDT at the time when the lobate scarps were formed. However, the heterogeneous insolation pattern on the surface of Mercury should induce, for a given time, differences in lithospheric strength and BDT depth depending on latitude and longitude (Williams et al., 2011), even for an evenly distributed mantle heat flow and crustal thickness. The difference in surface temperature between the location of the scarps in the Kuiper region and that of Discovery Rupes (currently about ~70 K according to the temperature model of Vasavada et al., 1999) would imply a slightly shallower BDT depth for the former, although our results do not have sufficient resolution to clearly reveal this difference. Alternatively, the formation of the scarps analyzed in the three regions might not have been contemporaneous, and therefore not indicative of the BDT depth at a single period of time.

Our results are consistent with the predictions of thermal history models for the range of time relevant for scarp formation. The obtained BDT depths for the Kuiper region are roughly consistent with predictions for an equatorial hot pole (T_s=427 K) from the model of Williams et al. (2011) with dry diabase and dry olivine rheologies for the crust and mantle, respectively. Similarly, our surface heat flow values are consistent with ~20–30 $mW\,m^{-2}$ derived by Hauck et al. (2004) from a thermo-chemical evolution model in a formational scenario dominated by condensation processes. Our values also overlap with the values calculated, for the period relevant for lobate scarp formation, using the thermal history model of Williams et al. (2011) and HPE abundances based on silicate vaporization, condensation and CI chondritic compositions model (Table 2). The model tracks the changes in the mantle temperatures over time resulting from the internal heating from the radioactive decay of HPE, and the exchange of heat across the conductive boundary layers of the core–mantle boundary and the stagnant lid. The model accounts for variations in stagnant lid thickness that develop from the heterogeneous average near-surface temperatures predicted by Vasavada et al. (1999), which results in lateral BDT depth variations. Details of the model can be found by Williams et al. (2007, 2011) and references therein. The incompatible radiogenic elements are the primary source of heat generation in the crust and mantle and their concentration and distribution will influence heat flow within the lithosphere. Due to their affinity to melt, they will be preferentially concentrated in the crust and we show surface heat flow results in Table 2 for two end-member cases: all HPE partitioned into the crust and equal concentrations in the mantle and crust.

On the other hand the uncertainty in topography resolution could affect our results, somewhat expanding the range of acceptable results. Whereas the vertical resolution is good for the S_K3 and S_K4 scarps; uncertainties are larger for Santa Maria Rupes. However, as above noted, the profile across Santa Maria Rupes was modified in order to eliminate an impact crater in the back of the lobate scarp, which postdates scarp formation. Thus, we consider our results for Santa Maria Rupes less robust.

Future observations by the MESSENGER and BepiColombo missions will provide the necessary information about Mercury, to allow for improved constraints on the compositional and mechanical properties of the lithosphere, as well as their temporal and regional variations, that will result in furthering our understanding of the thermal evolution of this planet.

Acknowledgments

We thank Matthias Grott and an anonymous reviewer for their comments and suggestions. This work has been partly funded by the project AyA2009-08011 of the Spanish MICINN. IEG is thankful to the Spanish MICINN for support through Grant ESP2006-02934. JR work was supported by a contract Ramón y Cajal co-financed from the Ministerio de Ciencia e Innovación of Spain and the Fondo Social Europeo (ESF).

References

Aharonson, O., Zuber, M.T., Solomon, S.C., 2004. Crustal remanence in an internally magnetized non-uniform shell: a possible source for Mercury's magnetic field? Earth Planet. Sci. Lett. 218, 261–268.

Beardsmore, G.R., Cull, J.P., 2001. Crustal Heat Flow. A Guide to Measurement and Modelling. Cambridge University Press, Cambridge 324 pp.
Bonner, J.L., Blackwell, D.D., Herrin, E.T., 2003. Thermal constraints on earthquake depths in California. Bull. Seismol. Soc. Am. 93, 2333–2354.
Cordell, B.M., Strom, R.G., 1977. Global tectonics of Mercury and the Moon. Phys. Earth Planet. Inter. 15, 146–155.
Denevi, B.W., Robinson, M.S., Solomon, S.C., Murchie, S.L., Blewett, D.T., Domingue, D.L., McCoy, T.J., Ernst, C.M., Head, J.W., Watters, T.R., Chabot, N.L., 2009. The evolution of Mercury's crust: a global perspective from MESSENGER. Science 324, 613–618.
Grott, M., Hauber, E., Werner, S.C., Kronberg, P., Neukum, G., 2007. Mechanical modelling of thrust faults in the Thaumasia region, Mars, and implications for the Noachian heat flux. Icarus 186, 517–526.
Harmon, J.K., Campbell, D.B., Bindschadler, D.L., Head, J.W., Shapiro, I.I., 1986. Radar altimetry of Mercury: a preliminary analysis. J. Geophys. Res. 91, 385–401.
Hauck, S.A., Dombard, A.J., Phillips, R.J., Solomon, S.C., 2004. Internal and tectonic evolution of Mercury. Earth Planet. Sci. Lett. 222, 713–728.
Head, J.W., Murchie, S.L., Prockter, L.M., Robinson, M.S., Solomon, S.C., Strom, R.G., Chapman, C.R., Watters, T.R., McClintock, W.E., Blewett, D.T., Gillis-Davis, J.J., 2008. Volcanism on Mercury: evidence from the First MESSENGER Flyby. Science 321, 69–72.
Lin, J., Stein, R.S., 2004. Stress triggering in thrust and subduction earthquakes, and stress interaction between the southern San Andreas and nearby thrust and strike-slip faults. J. Geophys. Res. 109, B02303. doi:10.1029/2003JB002607.
Mackwell, S.J., Zimmerman, M.E., Kohlstedt, D.L., 1998. High-temperature deformation of dry diabase with application to tectonics on Venus. J. Geophys. Res. 103, 975–984.
Melosh, H.J., McKinnon, W.B., 1988. The tectonics of Mercury. In: Vilas, F., Chapman, C.R., Matthews, M.S. (Eds.), Mercury, pp. 374–400.
Mitchell, D.L., de Pater, I., 1994. Microwave imaging of Mercury's thermal emission at wavelengths from 0.3 to 20.5 cm. Icarus 110, 2–32.
Morgan, J.W., Anders, E., 1980. Chemical composition of Earth, Venus, and Mercury. Proc. Natl. Acad. Sci. USA 77, 6973–6977.
Nimmo, F., Watters, T.R., 2004. Depth of faulting on Mercury: implications for heat flux and crustal and effective elastic thickness. Geophys. Res. Lett., 31. doi:10.1029/2003GL018847.
Peplowski, P.N., Evans, L.G., Blewett, D.T., Denevi, B.W., Lawrence, D.J., Nittler, L.R., Rhodes, E.A., Solomon, S.C., 2011. Surface abundances of K, Th, and U on Mercury and implications for planet formation and evolution. In: Proceedings of the 42nd Lunar Planetary Science Conference, Abstract 2290.
Ranalli, G., 1997. Rheology of the lithosphere in space and time. Geol. Soc. Spec. Publ. 121, 19–37.
Ritzer, J.A., Hauck, S.A., Barnouin, O.S., Solomon, S.C., Watters, T.R., 2010. Mechanical structure of Mercury's lithosphere from MESSENGER Observations of Lobate Scarps. In: Proceedings of the 41st Lunar Planetary Science Conference, Abstract 1533.
Ruiz, J., McGovern, P.J., Tejero, R., 2006. The early thermal and magnetic state of the cratered highlands of Mars. Earth Planet. Sci. Lett. 241, 2–10.
Ruiz, J., Fernández, C., Gomez-Ortiz, D., Dohm, J.M., López, V., Tejero, R., 2008. Ancient heat flow, crustal thickness, and lithospheric mantle rheology in the Amenthes region Mars. Earth and Planet. Sci. Lett. 270, 1–12.
Ruiz, J., Williams, J.P., Dohm, J.M., Fernández, C., López, V., 2009. Ancient heat flow and crustal thickness at Warrego rise, Thaumasia highlands, Mars: implications for a stratified crust. Icarus 203, 47–57.
Schubert, G., Ross, M.N., Stevenson, D.J., Spohn, T., 1988. Mercury's thermal history and the generation of its magnetic field. In: Vilas, F., Chapman, C.R., Matthews, M.S. (Eds.), MercuryUniversity. of Arizona Press, Tucson, pp. 429–460.
Schultz, R.A., Watters, T.R., 2001. Forward mechanical modeling of the Amenthes Rupes thrust fault on Mars. Geophys. Res. Lett. 28, 4659–4662.
Smith, D.E., Zuber, M.T., Phillips, R.J., Solomos, S.C., Neumann, G.A., Lemoine, F.G., Torrence, M.H., Peale, S.J., Margot, J.-L., Barnouin-Jha, O.S., Head, J.W., Talpe, M., 2010. The equatorial shape and gravity field of Mercury from MESSENGER flybys 1 and 2. Icarus 209, 88–100.
Strom, R.G., Trask, N.J., Guest, J.E., 1975. Tectonism and volcanism on Mercury. J. Geophys. Res. 80, 2478–2507.
Tanaka, K.P., Hartmann, W.K., 2008. The planetary timescale. In: Ogg, Ogg, G.M., Gradsteim., F.M. (Eds.), The Concise Geologic Time ScaleCambridge University Press, New York, pp. 13–22.
Taylor, G.J., Scott, E.R.D., 2005. Mercury. Treatise on Geochemistry, vol. 1. Elsevier, ISBN: 0-08-044720-1, p. 477.
Tesauro, M., Kaban, M.K., Cloetingh, S.A.P.L., Hardebol, N.J., Beekman, F., 2007. 3D strength and gravity anomalies of the European lithosphere. Earth Planet. Sci. Lett. 263, 56–73.
Toda, S., Stein, R.S., Richards-Dinger, K., Bozkurt, S., 2005. Forecasting the evolution of seismicity in southern California: animations built on earthquake stress transfer. J. Geophys. Res. 110, B05S16. doi:10.1029/2004JB003415.
Turcotte, D.L., Schubert, G., 2002. GeodynamicsCambridge University Press, Cambridge.
Vasavada, A.R., Paige, D.A., Wood, S.E., 1999. Near-surface temperatures on Mercury and the Moon and the stability of polar ice deposits. Icarus 141, 179–193.
Watters, T.R., Cook, A.C., Robinson, M.S., 2001. Large-scale lobate scarps in the southern hemisphere of Mercury. Planet. Space Sci. 49, 1523–1530.
Watters, T.R., Schultz, R.A., Robinson, M.S., Cook, A.C., 2002. The mechanical and thermal structure of Mercury's early lithosphere. Geophys. Res. Lett., 29. doi:10.1029/2001GL014308.
Watters, T.R., Nimmo, F., 2010. The tectonics of Mercury. In: Watters, T.R., Schultz., R.A. (Eds.), Planetary TectonicsCambridge University Press, Cambridge, pp. 15–80.
Williams, J.P., Aharonson, O., Nimmo, F., 2007. Powering Mercury's dynamo. Geophys. Res. Lett. 34, L21201. doi:10.1029/2007GL031164.
Williams, J.P., Ruiz, J., Rosenburg, M.A., Aharonson, O., Phillips, R.J., 2011. Solar insolation driven variations of Mercury's lithospheric strength. J. Geophys. Res. 116, E01008. doi:10.1029/2010JE003655.